ISSN 0027-1349, Moscow University Physics Bulletin, 2024, Vol. 79, Suppl. 2, pp. S906–S913. © Allerton Press, Inc., 2024.

Machine Learning for FARICH Reconstruction at NICA SPD

F. Shipilov[1,2*], A. Barnyakov[3,4], A. Ivanov[5], and F. Ratnikov[1]

[1] *HSE University, Moscow, Russia*
[2] *Skoltech, Moscow, Russia*
[3] *Budker Institute of Nuclear Physics, Siberian Branch, Russian Academy of Sciences, Novosibirsk, Russia*
[4] *Novosibirsk State Technical University, Novosibirsk, Russia*
[5] *Joint Institute for Nuclear Research, Dubna, Moscow oblast, Russia*
Received October 1, 2024; revised October 10, 2024; accepted October 20, 2024

Abstract—In the end-cap region of the SPD detector complex, particle identification will be provided by a Focusing Aerogel RICH detector (FARICH). FARICH's primary function is to separate pions and kaons in final open charmonia states (momenta below 5 GeV/c). The optimization of detector parameters, as well as a free-running (triggerless) data acquisition pipeline to be employed in the SPD necessitate a fast and robust method of event reconstruction. In this work, we employ a Convolutional Neural Network (CNN) for particle identification in FARICH. The CNN model achieves a superior separation between pions and kaons compared with traditional approaches. Unlike algorithmic methods, an end-to-end CNN model is able to process a full 2-dimensional detector response and skip the intermediate step of computing particle velocity, solving the particle classification task directly.

Keywords: NICA SPD, FARICH, machine learning, particle identification

DOI: 10.3103/S0027134924702369

1. INTRODUCTION

The Spin Physics Detector (SPD) is a universal detector proposed by the SPD collaboration at the Nuclotron-based Ion Collider fAcility (NICA) to study the Drell–Yan (DY) processes, J/Ψ production processes, elastic reactions, spin effects in one and two hadron production processes, polarization effects in heavy ion collisions, and more (Fig. 1, left) [1]. The SPD is a medium energy experiment, offering unique possibilities of beam operation and bridging the gap between the low-energy measurements, e.g. ANKE-COSY [2] and the high-energy measurements, such as Relativistic Heavy Ion Collider [3]. Several design peculiarities arise from the unique goals of the project. High luminosity up to 10^{32} cm^{-2} s^{-1} and free-flowing (triggerless) running mode require novel approaches to the data acquisition [4].

The experimental high-energy physics (HEP) objectives require searching for rare signals in background dominated environments. Machine learning techniques can extract high-level representations from the input data and model complex relations while providing excellent scalability and ease of parallelization. Machine learning approaches are state-of-the-art across a diversity of HEP problems [5].

The SPD project employs machine learning for the trigger system and reconstruction of events in several stages of the data acquisition pipeline. Fast tracking is instrumental to the trigger system at the SPD. There is a rich history of successful applications of machine learning for these tasks. For example, boosted decision trees were implemented in FPGIs as a level-1 trigger system at the CMS experiment [6]. GEM tracking performance was substantially improved with neural networks [7, 8].

Originally, a time-of-flight (ToF) detector was exclusively considered for $\pi/K/p$ separation in the SPD experiment [1]. Recently, the addition of aerogel counter in the end-cap region was proposed to improve π/K-separation [9, 10]. This opens up unique opportunities for machine learning applications as well. Machine learning has already been successfully applied to calibration and reconstruction of Cherenkov detectors [11].

*E-mail: foma@shipilov.ru

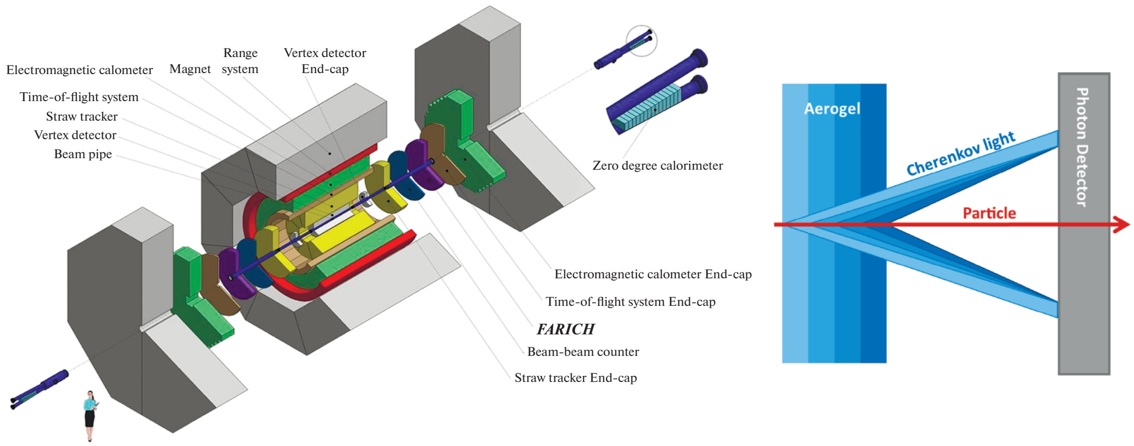

Fig. 1. Left to right: FARICH in the SPD experiment [10], aerogel detector layout [12].

In this work, we develop several models for fast reconstruction of the NICA SPD aerogel subsystem. In the Section 1, we analyze existing literature and list the main requirements for FARICH in NICA SPD setting. Section 2 describes the methods employed in the FARICH reconstruction. Section 3 outlines the experimental results and Section 5 discusses important questions arising from the analysis and future directions.

1.1. FARICH Detector

Ring-imaging Cherenkov (RICH) detectors use Cherenkov photons to measure the velocities of elementary particles needed for the particle identification. Whenever a particle travels at a velocity higher than the speed of light in the medium, Cherenkov radiation is generated. Cherenkov photons form a cone that imprints an elliptically shaped signal on a flat detector surface. A well-known relation between the velocity of a particle and the Cherenkov angle is as follows:

$$\beta = \frac{1}{n \cos \theta_c}, \tag{1}$$

where β denotes the particle velocity in units of c, n is the refractive index of the medium, and θ_c is the Cherenkov angle.

The main components of the RICH detector are a radiator and a photomultiplier (PM) array. Due to the finite size of the radiator, the Cherenkov cone vertex traverses the full thickness of the radiator during the passage of the particle. Proximity-focusing (proximity-imaging, nonfocusing) aerogel detectors compensate for this in the reconstruction stage [13]. However, if a high resolution is desired, Cherenkov photons must be focused to reduce variance of the signal. Focusing mirrors can be employed to reflect the photons back to the PM array, however, they are difficult and expensive to install and maintain, and require larger space, which is absent in colliding beams experiments [14].

Aerogel has seen extensive use as a radiator material for as soon as high quality samples appeared on the market. The main idea behind the Focusing Aerogel RICH (FARICH) detector is stacking several layers of aerogel with increasing refractive index (Fig. 1, right). Thus, the focusing happens inside the radiator, eliminating the need for mirrors, drastically reducing the complexity [15].

Common RICH particle identification (PID) methods are based on calculating various statistics of the Cherenkov angle distribution. RICH PID in the LHCb [16] and AMS [13] experiments is performed by discriminating mass hypotheses via a maximum likelihood estimation. Prior particle track info and detector response are used to determine Cherenkov angles for each photon hit and compute PID statistics. Belle II experiment adopts an approximation of the Cherenkov angle distribution with a Gaussian [15].

1.2. NICA SPD FARICH Requirements

The aerogel counter in the SPD project is expected to provide π/K-separation in the momenta range is below 5 GeV/c, necessitating a focusing aerogel (FARICH) [9]. A robust reconstruction of events in FARICH is required, i.e., identifying the correspondence between tracks supplied by the online trigger and Cherenkov rings.

There are 2 possible cases: the use of silicon photo-multipliers (SiPMs) or microchannel plate detectors (MCPs). The SPD is characterized by long bunches up to 76 ns [9]. In the first case, this results in a significant background rate which should be countered with some kind of software algorithm, possibly employing machine learning techniques.

In the second case, the problem of superimposed Cherenkov rings arises. It is expected that the geometric coordinates of the Cherenkov cone vertices will be known with sufficient precision. It follows that the error will be localized in the time domain.

Unfortunately, the tracking system is too slow for the application of hardware reconstruction. A purely software-based approach would need to find a matching between rings, tracks and vertices. It is argued that machine learning may help to speed up the computation compared with a brute-force approach.

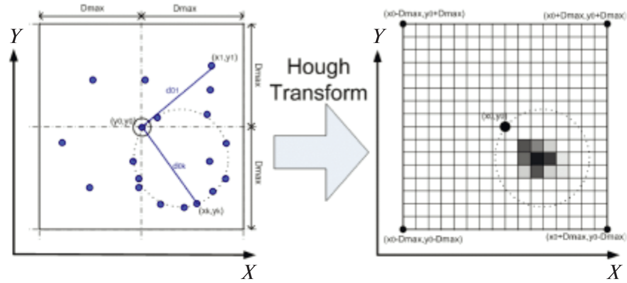

Fig. 2. RICH Hough transform baseline [17].

2. METHODOLOGY

In the task of FARICH reconstruction, one is generally provided with the following inputs:

- Track parameters: x_p, y_p, z_p—coordinates of the particle upon entering the aerogel, θ_p, ϕ_p—polar angle and azimuth of the direction of travel;
- Photon hits: x_c, y_c, z_c—coordinates of triggered pixels in the photosensitive matrix.

The SiPMs used in the matrix can be triggered by Cherenkov photons, as well as background radiation and intrinsic noise.

Our baseline for the single ring reconstruction was based on the RICH reconstruction from CBM experiment at FAIR [17]. The algorithm utilizes Hough transform for ellipses, more precisely the Taubin method [18]. The Hough transform outputs estimated parameters of the ellipse, such as a, b—semiaxes, x, y—center coordinates, and ϕ—angle of rotation (Fig. 2). These parameters are then used to calculate θ_c (1). It is important to note that the baseline was fixed, so we only had access to the precomputed θ_c values. The baseline does not account for refraction in the aerogel, but most importantly, it does not have access to the information from the straw tracker, such as θ_p and ϕ_p.

2.1. Refraction Correction

Cherenkov photons are refracted upon exiting the radiator (Fig. 3), making a direct computation of θ_c from x_c, y_c inaccurate. Therefore, it is necessary to undo the refraction and obtain the unaffected θ_c values.

Let α be the angle of incidence, β be the angle of reflection, n be the refractive index of the aerogel. Then

$$\begin{cases} d\tan\beta + h\tan\alpha = r \\ n\sin\alpha = \sin\beta. \end{cases} \tag{2}$$

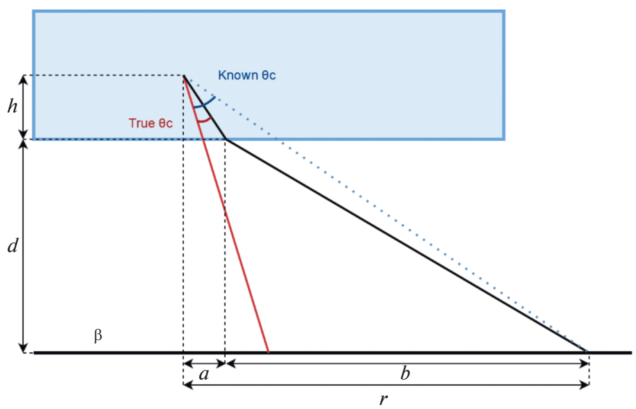

Fig. 3. Exit refraction in the radiator.

One can find α if β is known using (2), for example, using first order approximation or fixed-point iteration. In the first order approximation $\beta = \alpha + \Delta\alpha$, $\Delta\alpha \ll \alpha$, $h \ll d$. Then

$$\alpha \approx \beta - (n-1)\tan\beta.$$

The fixed-point iteration step is

$$\sin\alpha_{k+1} = \left(n\sqrt{1 + \left(\frac{d}{r - h\tan\alpha_k}\right)^2}\right)^{-1}.$$

With initial value

$$\sin\alpha_0 = r/\sqrt{r^2 + (d+h)^2}.$$

Fixed point iteration achieves slightly better approximation; however, it requires more computations. Figure 4 demonstrates how θ_c becomes constant with respect to azimuth ϕ_c after refraction correction.

2.2. Algorithmic Models

The values of θ_c were used to estimate $\hat{\theta}_c$ with several approaches. The first model (median) computes the median of θ_c after correction. The second model (maximum likelihood, MLE) finds the mode of the distribution using a numerical derivative.

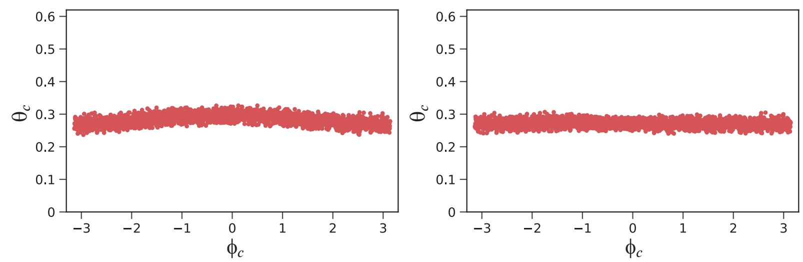

Fig. 4. Left—Cherenkov angles before correction, right—after.

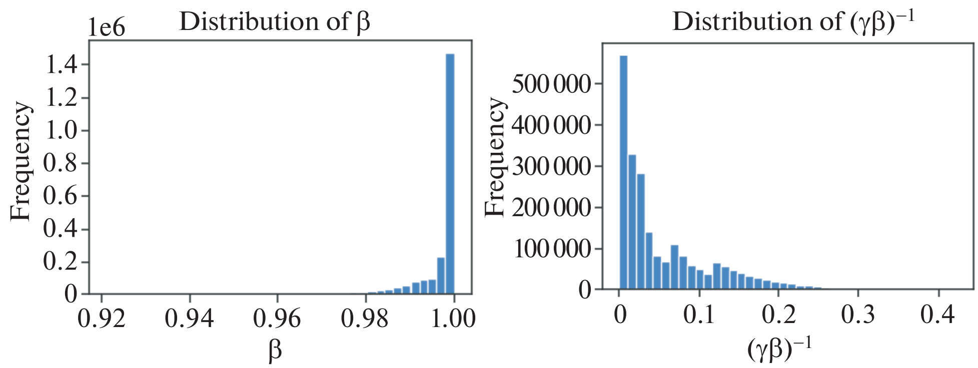

Fig. 5. β distribution in the data. The sample is heavily skewed because of the relativistic electrons produced in collisions.

2.3. Machine Learning Models

Algorithmic models output $\hat{\theta}_c$ that can be converted to the rest mass of the particle using the absolute value of momentum p from the straw tracker. In ML terms, these are regression models. However, the objective of RICH detector is to separate different particle types, in particular, FARICH should improve π/K-separation. This can be formulated as a classification problem.

Unlike algorithmic models, ML end-to-end models are able to skip the intermediate step of computing $\hat{\beta}$. Moreover, the regression task is not well suited for an ML model because of the significant value imbalance (Fig. 5, left). Generally, the momentum distribution is expected to be close to uniform, which results in very high velocities for low mass particles, e.g., electrons. One possible mitigation is to compensate β with Lorenz factor γ prior to feeding it into the model (Fig. 5, right), but the distribution is still far from being properly balanced.

Taking this into account, we implemented a neural classifier that incorporated both hit coordinates x_c, y_c and momentum p information. There were 2 possible approaches: either to provide the value of p as an extra input channel/pathway in the neural network, or to employ it in normalizing the input data. In our case, the nonlinear dependence on p could be disentangled before applying classifier model. The following relation stands:

$$\cos\theta_c = \frac{1}{n}\sqrt{m_0^2/p^2 + 1}, \tag{3}$$

where m_0 is the rest mass. This approach is beneficial by that it frees the model from learning this nonlinear relationship implicitly, enabling more efficient use of the model's computational power.

The classification was performed by first correcting for refraction and using (3) with N mass probes for each of the particle types in the data to transform θ_c into β-independent space, then splitting the input into N channels, each with x_c, y_c recomputed using the corresponding mass probe.

Surely, by multiplying $\cos\theta_c$ by an inverse of (3), one obtains $\cos\theta_c = 1$, provided m_0 is matching the true rest mass of the particle in the data, and $\cos\theta_c \neq 1$ otherwise. As a result, a fixed size Cherenkov ring is placed in the channel corresponding to the correct particle, while rings of different sizes are in other channels. In theory, by thresholding this known fixed size, all channels except the correct one can be cleared of the hits entirely. In practice, this threshold can not be made very small because of the finite thickness of the Cherenkov ring. We tuned the threshold value so that it did not drop too much relevant hits for the correct mass probe, but still eliminated them for the wrong probes (Fig. 6).

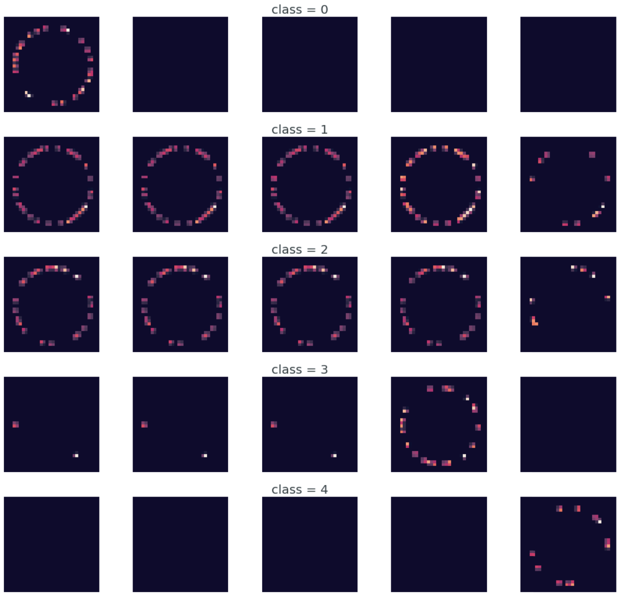

Fig. 6. Classifier input example. Almost perfect identification of e^-, K^+, p (classes 0, 3, 4) is achieved already during this stage.

3. NUMERICAL EXPERIMENTS

The dataset in question was compiled using Geant4 particle passage simulation toolkit and contained 5 366 595 simulated events. 5 particles were present in the data in similar quantities: e^-, μ^-, π^+, K^+, and p. The data consisted solely of Cherenkov photons and did not include background hits and scattered photons. High quality photomultipliers are planned for use in the NICA SPD FARICH, so the real background rate should be fairly low.

The dataset contained events with low β values that did not produce any Cherenkov photons (Fig. 5). There were also events with unphysical $\theta_p > \pi/2$ indicating that particles were moving backwards through the detector. We excluded these events from our analysis, because they led to a breakdown of all reconstruction algorithms. In total, such events accounted for a 1.7% of the dataset.

We reserved 20 000 events for testing, 5000 for validation, and used the remaining for model training and calibration. The input format for NN classifier was a $5 \times 32 \times 32$ tensor, each 32×32 channel containing a mass probe for a corresponding particle. A custom ResNet-18 network was used as a classifier with changes to the input convolution, max pooling and classifier head to accommodate for the input and output formats. It was trained on 200 000 samples with Adam optimizer, cosine annealing scheduler, a learning rate of 5×10^{-4} and a batch size of 128. Multiclass accuracy, precision, recall and AUROC were monitored during training.

3.1. Regression Metrics

First, we evaluated the algorithmic models' performance using regression metrics. Median had the lowest standard deviation σ_β, followed by MLE and then Hough baseline (Fig. 7). However, there was a systematic bias in the predictions. Fortunately, the bias was very linear, thus could be corrected by a simple transform. The systematic correction transform parameters were computed on a training set and applied to the predictions. This improved σ_β by more than 40% for median. MLE estimate also improved, however, Hough baseline standard deviation increased. A possible reason for this can be found in Section 4. Nevertheless, the mean value of the residuals improved, therefore we used corrected values in the subsequent analysis.

3.2. Classification Metrics

For algorithmic models rest masses were computed from the predictions of each method. Particle types were assigned based on the predictions proximity to true rest masses. For NN model, logits and predicted classes were computed directly.

The results were summarized in the Table 1. In the case of π/K-separation metrics, a subset of the test data was taken with only π and K classes.

Median demonstrated the best separation overall and the best π/K-separation of all algorithmic models, but was still outperformed by the NN model. Hough baseline had lower K false positive rate than MLE at the cost inferior performance along the rest of the metrics.

Our algorithmic methods were different from the baseline because we carefully accounted for refraction, producing sharper θ_c distribution. The other disadvantage of Hough transform was its high dimensionality in the case of ellipses (5 parameters). While Hough transform worked reliably for simple circles, it had challenges locating ellipses precisely. Nevertheless, the gravest difference was having access to the particle track.

The multiclass accuracy of all methods, including NN, was not very high because lower mass particles were not separated well (Fig. 8). Nevertheless, in the case of NN and median it did not impede π/K-separation, which is more important. On the contrary, MLE, and, exceedingly, Hough, struggled with it. Protons were separated well in all methods.

One possible explanation behind excellent quality of the NN model is that it had access to additional spatial information that was unavailable in algorithmic approaches. It could utilize it to achieve better performance. Another possible advantage is the end-to-end training process, optimizing classification performance rather than intermediate regression metrics.

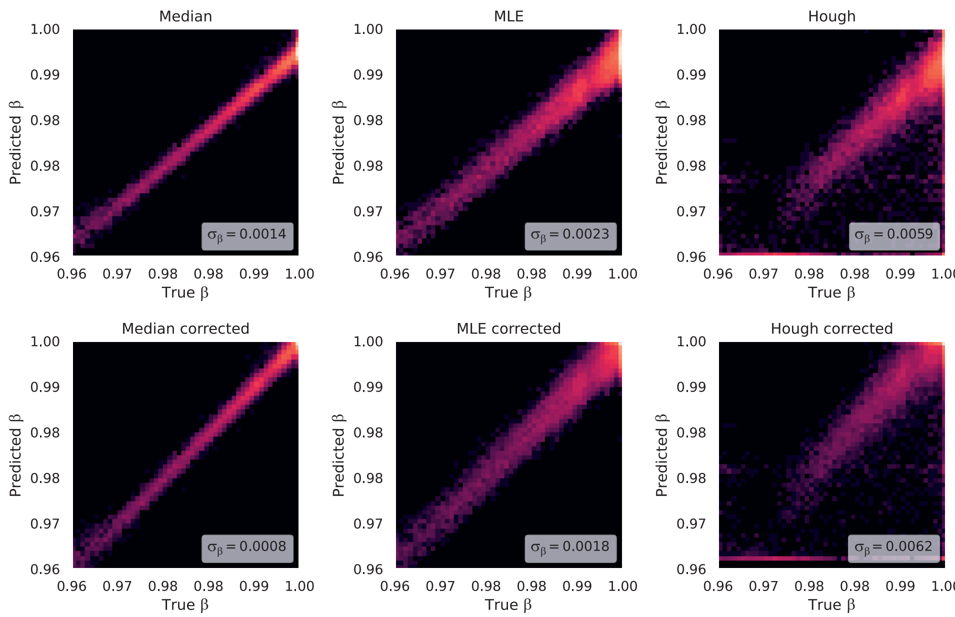

Fig. 7. Test set 2D correlation plots for algorithmic models before (top) and after systematic correction (bottom).

Table 1. Classification metrics on the test set. NN model outperforms the best algorithmic model, particularly in π/K-separation. The errors denote 95% CI in an assumption of normally distributed mass predictions for each class

Method	$\mathbb{P}$(true π, pred K)	$\mathbb{P}$(true K, pred π)	π, K AUROC	Total accuracy	σ_β
NN	$\mathbf{0.016 \pm 0.005}$	$\mathbf{0.010 \pm 0.005}$	**0.997**	**0.65**	**N/A**
Median	0.06 ± 0.02	0.02 ± 0.02	0.989	0.64	0.0008
MLE	0.20 ± 0.02	0.12 ± 0.02	0.883	0.52	0.0018
Hough	0.13 ± 0.02	0.26 ± 0.02	0.817	0.49	0.0062

4. ABLATION STUDY

We investigated the performance of our methods by removing both refraction and systematic corrections. Surprisingly, median computed using raw θ_c before refraction correction produced lower σ_β than the corrected one (Fig. 9, left). However, when corrected for systematic bias, the advantage was lost. Despite better initial bias, the variance of the model was higher from the beginning.

This also explains why the quality of Hough baseline decreased after systematic correction. The bias was introduced by the refraction correction algorithm. Hough baseline does not account for refraction and thus demonstrates better compliance initially.

In another test we computed the mass distribution using median values without systematic correction. π/K-separation suffered immensely, with false positive and negative rates in the range of 50% and higher (Fig. 9, right).

The ablation study provided largely positive evidence that the corrections were necessary to achieve the reported quality.

5. DISCUSSION AND CONCLUSION

ML-based approaches have gained attention of physicists across many different research fields. In particular, applications in particle and nuclear physics, ranging from experiment design to fast experimental data processing, offer great prospects for enabling new scientific discoveries [19]. Deep Learning applications have been recently explored in the context of fast and reliable reconstruction and simulation of RICH detectors. In particular, neural networks used for fast reconstruction offer higher reconstruction accuracy and robustness.

The process of developing the FARICH detector for NICA SPD gives rise to several tasks with high potential for ML application, such as particle identification and track matching. In this work, we developed and tested single ring reconstruction methods for NICA SPD FARICH. The initial results of applying ML were promising, with a lot of useful implications and potential for future studies. While our NN model achieved good accuracy, it is too large

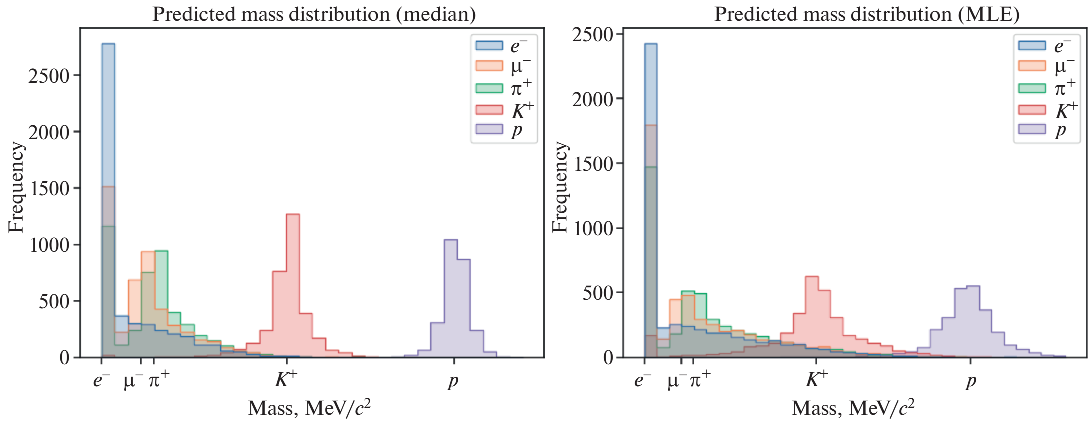

Fig. 8. Predicted mass distribution, color coded by true classes.

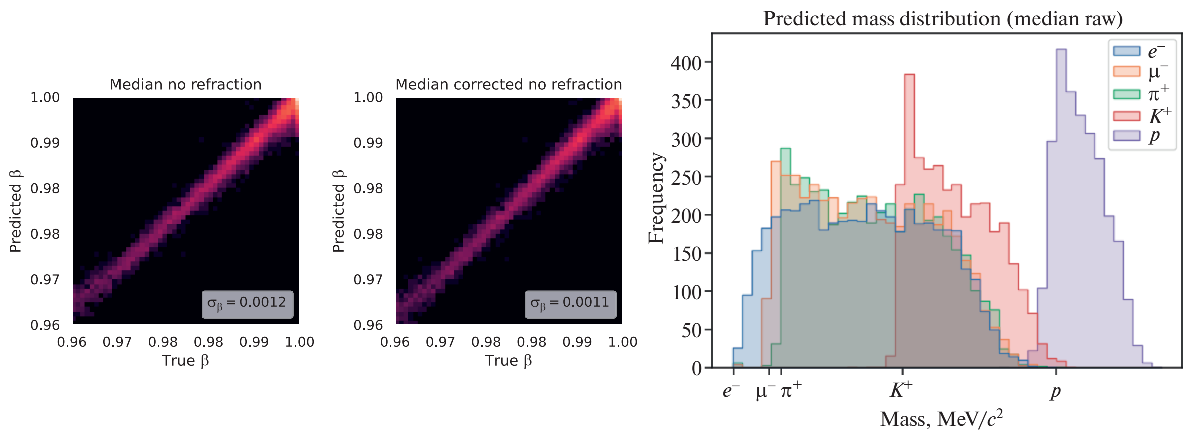

Fig. 9. Ablation study. Left to right: test set 2D correlation without any correction; with systematic, but without refraction correction; predicted mass distribution with refraction, but without systematic correction.

to use in the real time processing. Moreover, by far the most computationally expensive part of the pipeline was the forming of input probes that are then fed into NN.

The logical next step would be to optimize the architecture with various techniques, such as knowledge distillation, pruning and quantization with a a multi layer perceptron (MLP) as a target architecture. It is also essential to narrow down the exact parameters of the system, such as the probability of ring overlap, background and intrinsic noise intensity, and the scattering of Cherenkov photons. After that, we can develop more realistic models with multi-ring methods and, eventually, the real time trigger for track-ring matching.

FUNDING

The research leading to these results has received funding from the Basic Research Program at the National Research University Higher School of Economics.

CONFLICT OF INTEREST

The authors of this work declare that they have no conflicts of interest.

REFERENCES

1. I. Savin, A. Efremov, D. Pshekhonov, A. Kovalenko, O. Teryaev, O. Shevchenko, A. Nagajcev, A. Guskov, V. Kukhtin, and N. Toplilin, Eur. Phys. J. A **52**, 215 (2016).
https://doi.org/10.1140/epja/i2016-16215-x
2. M. Mikirtychyants, R. Engels, K. Grigoryev, A. Vasilyev, D. Chiladze, A. Kacharava, S. Mikirtychyants, F. Rathmann, J. Sarkadi, R. Schleichert, H. Seyfarth, H. Stroeher, D. Prasuhn, B. Lorentz, S. Barsov, and S. Dymov, J. Phys.: Conf. Ser. **295**, 012148 (2011).
https://doi.org/10.1088/1742-6596/295/1/012148
3. B. Müller and J. L. Nagle, Ann. Rev. Nucl. Part. Sci. **56**, 93 (2006).
https://doi.org/10.1146/annurev.nucl.56.080805.140556

4. V. M. Abazov, V. Abramov, L. G. Afanasyev, R. R. Akhunzyanov, A. V. Akindinov, N. Akopov, I. G. Alekseev, A. M. Aleshko, V. Yu. Alexakhin, G. D. Alexeev, M. Alexeev, A. Amoroso, I. V. Anikin, V. F. Andreev, V. A. Anosov, A. B. Arbuzov, N. I. Azorskiy, A. A. Baldin, V. V. Balandina, E. G. Baldina, M. Yu. Barabanov, S. G. Barsov, V. A. Baskov, A. N. Beloborodov, I. N. Belov, A. P. Belova, A. V. Belyaev, A. Ya. Berdnikov, Ya. A. Berdnikov, A. V. Berezhnoy, V. V. Bleko, A. V. Bobkov, D. N. Bogoslovsky, I. N. Boguslavsky, E. V. Boltushkin, E. E. Boos, V. E. Burtsev, L. Chen, A. S. Chepurnov, M. Chiosso, et al., arXiv Preprint (2021).
https://doi.org/10.48550/arXiv.2102.00442
5. K. Albertsson, P. Altoe, D. Anderson, M. Andrews, J. P. Araque Espinosa, A. Aurisano, L. Basara, A. Bevan, W. Bhimji, D. Bonacorsi, P. Calafiura, M. Campanelli, L. Capps, F. Carminati, S. Carrazza, T. Childers, E. Coniavitis, K. Cranmer, C. David, D. Davis, J. Duarte, M. Erdmann, J. Eschle, A. Farbin, M. Feickert, N. F. Castro, C. Fitzpatrick, M. Floris, A. Forti, J. Garra-Tico, J. Gemmler, M. Girone, P. Glaysher, S. Gleyzer, V. Gligorov, T. Golling, J. Graw, L. Gray, D. Greenwood, T. Hacker, J. Harvey, et al., J. Phys.: Conf. Ser. **1085**, 022008 (2018).
https://doi.org/10.1088/1742-6596/1085/2/022008
6. D. Acosta, A. Brinkerhoff, E. Busch, A. Carnes, I. Furic, S. Gleyzer, Kh. Kotov, J. F. Low, A. Madorsky, J. Rorie, B. Scurlock, and W. Shi, J. Phys.: Conf. Ser. **1085**, 042042 (2018).
https://doi.org/10.1088/1742-6596/1085/4/042042
7. D. Baranov, S. Mitsyn, P. Goncharov, and G. Ososkov, EPJ Web Conf. **214**, 06018 (2019).
https://doi.org/10.1051/epjconf/201921406018
8. G. A. Ososkov, O. V. Bakina, D. A. Baranov, P. V. Goncharov, I. I. Denisenko, A. S. Zhemchugov, Yu. A. Nefedov, A. V. Nechaevskiy, A. N. Nikolskaya, E. M. Shchavelev, L.-L. Wang, S.-S. Sun, and Ya. Zhang, Computer Research and Modeling **12**, 1361 (2020).
https://doi.org/10.20537/2076-7633-2020-12-6-1361-1381
9. V. Abazov, V. Abramov, L. Afanasyev, R. Akhunzyanov, A. Akindinov, I. Alekseev, A. Aleshko, V. Alexakhin, G. Alexeev, L. Alimov, A. Allakhverdieva, A. Amoroso, V. Andreev, V. Andreev, E. Andronov, Yu. Anikin, S. Anischenko, A. Anisenkov, V. Anosov, E. Antokhin, A. Antonov, S. Antsupov, A. Anufriev, K. Asadova, S. Ashraf, V. Astakhov, A. Aynikeev, M. Azarkin, N. Azorskiy, A. Bagulya, D. Baigarashev, A. Baldin, E. Baldina, N. Barbashina, A. Barnyakov, S. Barsov, A. Bartkevich, V. Baryshevsky, K. Basharina, A. Baskakov, V. Baskov, M. Batista, M. Baturitsky, V. Bautin, et al. (The SPD Collaboration), arXiv Preprint (2024).
https://doi.org/10.48550/arXiv.2404.08317
10. A. Korzenev (SPD Collaboration), in *Technology & Instrumentation in Particle Physics (TIPP2023), Cape Town, South Africa, 2023* (2023). https://indico.tlabs.ac.za/event/112/contributions/2962/attachments/1047/1479/korzenev_TIPP2023.pdf.
11. C. Fanelli, J. Instrum. **15**, C02012 (2020).
https://doi.org/10.1088/1748-0221/15/02/c02012
12. A. Yu. Barnyakov, J. Phys.: Conf. Ser. **1561**, 012004 (2020).
https://doi.org/10.1088/1742-6596/1561/1/012004
13. F. Barao, L. Arruda, J. Borges, P. Gonçalves, M. Pimenta, and I. Perez, Nucl. Instrum. Methods Phys. Res., Sect. A **502**, 310 (2003).
https://doi.org/10.1016/s0168-9002(03)00294-8
14. M. Alexeev, R. Birsa, F. Bradamante, A. Bressan, M. Chiosso, P. Ciliberti, S. Dalla Torre, O. Denisov, V. Duic, A. Ferrero, M. Finger, M. Finger, Jr., M. Giorgi, B. Gobbo, S. Levorato, A. Maggiora, A. Martin, G. Menon, D. Panzieri, G. Pesaro, J. Polak, E. Rocco, G. Sbrizzai, P. Schiavon, M. Slunecka, F. Sozzi, L. Steiger, M. Sulc, S. Takekawa, and F. Tessarotto, Nucl. Instrum. Methods Phys. Res., Sect. A **639**, 219 (2011).
https://doi.org/10.1016/j.nima.2010.10.149
15. H. Kindo, I. Adachi, L. Burmistrov, F. Le Diberder, K. Hataya, S. Kakimimoto, H. Kakuno, H. Kawai, T. Kawasaki, T. Konno, S. Korpar, P. Križan, T. Kumita, Y. Lai, M. Machida, M. Mrvar, S. Nishida, K. Noguchi, K. Ogawa, S. Ogawa, R. Pestotnik, L. Šantelj, T. Sumiyoshi, M. Tabata, S. Tamechika, M. Yonenaga, M. Yoshizawa, and Y. Yusa, Nucl. Instrum. Methods Phys. Res., Sect. A **952**, 162252 (2020).
https://doi.org/10.1016/j.nima.2019.05.093
16. A. Powell (LHCb RICH Collaboration), Nucl. Instrum. Methods Phys. Res., Sect. A **639**, 260 (2011).
https://doi.org/10.1016/j.nima.2010.09.048
17. S. A. Lebedev and G. A. Ososkov, Phys. Part. Nucl. Lett. **6**, 161 (2009).
https://doi.org/10.1134/s1547477109020095
18. N. Chernov, J. Math. Imaging Vision **27**, 231 (2007).
https://doi.org/10.1007/s10851-006-0646-1
19. A. Boehnlein, M. Diefenthaler, N. Sato, M. Schram, V. Ziegler, C. Fanelli, M. Hjorth-Jensen, T. Horn, M. P. Kuchera, D. Lee, W. Nazarewicz, P. Ostroumov, K. Orginos, A. Poon, X.-N. Wang, A. Scheinker, M. S. Smith, and L.-G. Pang, Rev. Mod. Phys. **94**, 31003 (2022).
https://doi.org/10.1103/revmodphys.94.031003